Congested shallow water model: on floating body

Edwige Godlewski, Martin Parisot, Jacques Sainte-Marie, Fabien Wahl

CONGESTED SHALLOW WATER MODEL: ON FLOATING BODY

EDWIGE GODLEWSKI, MARTIN PARISOT, JACQUES SAINTE-MARIE, AND FABIEN WAHL

Abstract. We consider the floating body problem in the vertical plane on a large space scale. More precisely, we are interested in the numerical modeling of body floating freely on the water such as icebergs or wave energy converters. The fluid-solid interaction is formulated using a congested shallow water model for the fluid and Newton's second law of motion for the solid. We make a particular focus on the energy transfer between the solid and the water since it is of major interest for energy production. A numerical approximation based on the coupling of a finite volume scheme for the fluid and a Newmark scheme for the solid is presented. An entropy correction based on an adapted choice of discretization for the coupling terms is made in order to ensure a dissipation law at the discrete level. Simulations are presented to verify the method and to show the feasibility of extending it to more complex cases.

1. Introduction

We are interested in the modeling of a floating body in the vertical plane. In a previous work [18], we considered a shallow water flow with an impermeable surface above it, namely the roof, which constrains the water surface. The roof is motionless or is given by an explicit time and space dependent function independent of the flow. In this work, we focus on a floating structure leading to the coupling of the equations on the fluid and on the motion of the structure. Applications are the drift of icebergs or flood debris, or the improvement of sustainable marine energy converters such as buoys.

Two main approaches are proposed in the literature to treat fluid-solid interaction. With the exception of work done in antiquity, in particular "On Floating Bodies" by Archimedes, the first one dates back to Fritz John who proposed a mathematical formulation of the problem [22]. The fluid is described by a velocity potential with a linear model for the free surface evolution. The motion of the solid is supposed to be of small amplitude so that the interface between the water and the solid is constant in time. Finally the surface pressure is obtained using the linearized Bernoulli equation. Although the model is quite simplified, linear potential flow theory is still used in industrial context since it is not costly in CPU time, see [30]. However nonlinear terms play an important part for wave interaction. For instance the non-linearity should be taken into account in simulations of wave energy converter farms. Improvements have been made to include an interface depending

Date: September 25, 2019.

2010 *Mathematics Subject Classification.* 35Q35, 70E15, 74F10, 76B07, 76M12.

Key words and phrases. shallow water equations, wave-body interaction, congested model, coupling, entropy satisfying scheme.

on time [23] and nonlinear effects based on the boundary element methods [20]. This progress needs higher CPU times and does not yet allow wave breaking.

The second approach involves Navier-Stokes CFD computations. This approach is considerably used in blood flow, for instance in aortic flow [36, 14]. Some other works also use Navier-Stokes CFD computations for the simulation of the flow around a yacht [34], fish [6] or wave energy converters [1, 31, 38]. In these works the fluid is expressed in an Eulerian frame while the solid is expressed in a Lagrangian frame. The difficulty comes from the mesh. A moving grid with front tracking methods or a fixed mesh with fictitious fluid domain can be considered. The first one perfectly catches the interface but needs a moving mesh while the second is less accurate on the position of the interface but the mesh is fixed. However this strategy implies high CPU times and does not make these methods suitable for engineering optimization. To take advantage of the benefits from each approach, a coupling has been proposed [37]. Since the viscosity is not considered in potential flow theory, it can hardly be included in the coupling.

Recently the nonlinear floating body problem was reformulated in the framework of vertical-integrated models [26]. A vertical movement of the body is considered so that the interface between the congested and the free surface domain is fixed in time and continuity of the unknowns is assumed at the interface. The surface pressure is then obtained by an elliptic equation. An analysis of this shallow water type model in the two dimensional case with radial symmetry is done in [7]. In [11], a phenomena of dispersive boundary layer is highlighted. In a more general framework the well-posedness of the model in the one dimensional case has been proven in [21], relaxing the assumption of vertical lateral walls. The description of the interface position is dealt with. A numerical resolution in one dimension is done in [10]. The free surface and the congested subdomain are solved using an appropriate numerical strategy, i.e. hyperbolic for the first and elliptic for the second. At the interfaces, the continuity of the pressure and the discharge is assumed. Unfortunately, the transmission condition is not clear physically, since a discontinuous solution is possible. In addition, when the position of the interface is also an unknown, the coupling strategy is tricky to handle, and not robust. In [18] we have proposed a uniform numerical resolution which eliminates the description of the interface and the transition conditions between the congested and the free surface domain. The surface pressure is seen as a Lagrange multiplier associated to a constraint. These models [18, 26] are based on depth-averaging and thus they cannot represent wave breaking but nonlinear terms are accounted for. Simpler than the Navier-Stokes equations but still physically relevant, their resolution is less CPU consuming since the computational domain does not depend on time. For optimization processes this seems interesting, especially when large domains are considered. Eventually the interaction of energy converters with the bottom as in [4, 5] can also be considered.

In the present work, we give a formulation of the problem taking into account a freely floating object in the vertical plane, i.e. two translations and one rotation. A choice of discretization for the different operators is proposed in order to ensure a strong coupling between the two systems. We use a Newmark scheme for the solid and adapt the numerical strategy given in [18] for a 'fixed roof' to the coupling. Furthermore our method allows to write the energy of the coupled fluid-solid system.

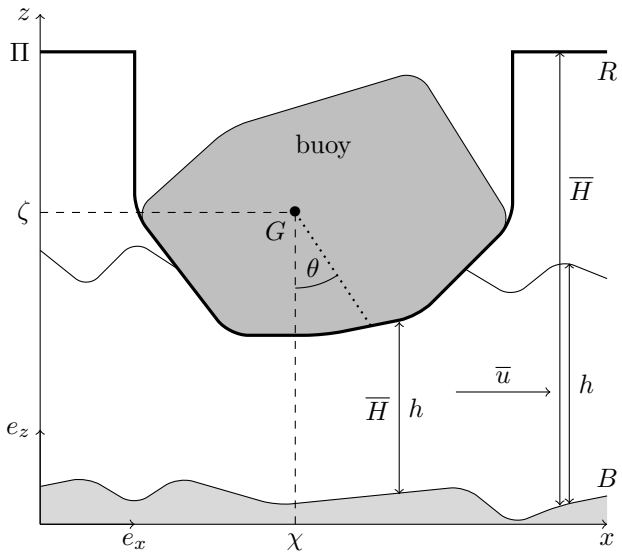

FIGURE 1. Floating body configuration and illustration of the unknowns.

The energy transfer between the fluid and the solid is indeed a challenging problem and of major interest in energy production using buoys. From a mathematical point of view, the energy balance, acting as an entropy, is an argument for the existence of long time solutions.

Note that the modeling of submerged objects is not allowed by the choice of modeling for the fluid since the vertical averaged model considers only one water height. Thus in the following, we will restrict ourselves to a certain type of configuration for the floating objects. More details are given in Hypothesis 2.

In Section 2 the formulation at the continuous level is given while Section 3 is dedicated to the numerical strategy. In both cases, the fluid and solid dynamics are considered separately, then the coupling is handled. At the discrete level, first a naive non-entropy satisfying approach is presented followed by an entropy correction. We also give details on the practical 1D implementation to treat general shapes of the floating body. Finally in Section 4 we show simulations to validate our approach.

2. Mathematical modeling

In the current section, a description of the governing equations of the floating body problem using a vertical-integrated model is given. The physical context is illustrated in Figure 1.

2.1. **Fluid dynamic.** In [18] a shallow water type model with an additional congestion constraint modeling a 'roof' is proposed. Let us briefly introduce this model which is derived from the Navier-Stokes equations. Let us consider the one dimensional domain $\Omega_x \subset \mathbb{R}$ where x stands for the horizontal coordinate in the frame of the observer and $t \in \mathbb{R}_+$ stands for the time variable. In practice the domain Ω_x will be bounded but for simplicity the boundary conditions will not be detailed. A flow contained between two surfaces (in the 1D framework, these are actually two

curves) respectively called roof and bottom is considered. The two surfaces can be parametrized by two given mono-valued functions $R(x,t)$, the roof, and $B(x,t)$, the bottom, which satisfy $B(x,t) \leq R(x,t)$. The surfaces must be regular enough where they are reached by the fluid, i.e. everywhere for the bottom and at least at the inferior surface of the floating body, see Hypothesis 1 below. The opening between the roof and the bottom is defined by $\overline{H}(x,t) = R(x,t) - B(x,t)$. The unknowns of the model are the water depth $h(x,t)$, the vertical-averaged horizontal velocity $\overline{u}(x,t)$ and the surface pressure $\overline{p}(x,t)$ which satisfy

$$\begin{cases} \partial_t h + \partial_x (h\overline{u}) = 0 \\ \partial_t (h\overline{u}) + \partial_x \left(h\overline{u}^2\right) = -h\partial_x \left(g(h+B) + \dfrac{\overline{p}}{\rho}\right) \end{cases} \tag{1}$$

with g the gravitational constant. The fluid is assumed to be homogeneous, then the water density ρ is constant in time and space and given. In addition, the congestion constraint

$$\min\left(\overline{H} - h, \overline{p} - P\right) = 0 \tag{2}$$

has to be satisfied where $P(x,t)$ denotes the given atmospheric pressure. In the following, the atmospheric pressure is taken constant in time and space and for simplicity equal to zero, i.e. $P = 0$. Finally the system (1)-(2) is completed with the initial conditions $h(x,0) = h^0(x)$ and $\overline{u}(x,0) = \overline{u}^0(x)$.

We recall the following energy balance law, the proof of which can be found in [18, Proposition 1.3].

Lemma 2.1. *Any smooth enough solution of the congested shallow water model (1)-(2) satisfies the following energy balance law*

$$\partial_t \mathcal{E} + \partial_x \mathcal{G} = -\overline{p}\partial_t R + (\rho g h + \overline{p})\,\partial_t B$$

with the mechanical energy and the energy flux respectively given by

$$\mathcal{E} = \frac{\rho}{2} h\overline{u}^2 + \rho g h\left(B + \frac{h}{2}\right) \qquad \text{and} \qquad \mathcal{G} = \left(\frac{\rho}{2}\overline{u}^2 + \rho g(h+B) + \overline{p}\right) h\overline{u}.$$

Unlike the work done in [18], if $B(x,t)$ is still a given function, this is no longer the case for $R(x,t)$. The interaction between the fluid and the roof is considered, i.e. $R(x,t)$ is now an unknown of the problem and its evolution has to be determined.

2.2. **Solid dynamic.** Let us describe the planar motion of a body subjected to the gravity field and a surface pressure force p. The reader can refer to [24] for more details about solid dynamics. In the vertical plane (e_x, e_z), the scalar product between two vectors $a = (a_1, a_2)$ and $b = (b_1, b_2)$ is denoted $a \cdot b = a_1 b_1 + a_2 b_2$ and the cross product $a \times b = a_1 b_2 - a_2 b_1$.

We describe a general planar movement of a homogeneous solid body by three degrees of freedom, denoted χ, ζ and θ, see Figure 1. The mass of the solid is denoted by M and its center of mass by $G = (\chi, \zeta)$, where $\chi \in \Omega_x$ denotes the horizontal and $\zeta \in \mathbb{R}$ the vertical component. The variable θ stands for the angle between the unit vector in the vertical direction e_z and the vector GX where X is a point in the solid different from the center of mass. The moment of inertia of the solid around an axis passing through the center of mass is denoted $\mathcal{J}$. We consider a solid subjected to gravity and a surface pressure of p. Additional horizontal (resp.

vertical) forces will be denoted by F_χ (resp. F_ζ) and their torque around the center of mass is denoted by T_θ.

Hereafter, we give the mathematical description of the buoy. Note that in practice, it needs a numerical implementation given in Section 3.4.1. For every $\theta \in [-\pi, \pi[$, the geometry of the solid body in the frame centered on G is the set of coordinates (x, z) satisfying $\mathcal{S}(x, z, \theta) = 0$, with $\mathcal{S}(x, z, \theta)$ a given function. In the context of a floating body, from now on called the buoy, the surface pressure only acts on its inferior surface. This inferior surface elevation is given by

$$z = \underline{\mathcal{S}}(x, \theta) = \min\{\widetilde{z} \in \mathbb{R} \mid S(x, \widetilde{z}, \theta) = 0\}$$

that leads to the following expression of $\mathcal{R}$, the inferior surface elevation in the frame of the observer

$$\mathcal{R}(x, \chi, \zeta, \theta) = \underline{\mathcal{S}}(x - \chi, \theta) + \zeta. \tag{3}$$

Note that $\mathcal{R}(x, \chi, \zeta, \theta)$ is not necessarily defined for all $(x, \chi, \zeta, \theta) \in \Omega_x \times \mathbb{R} \times \mathbb{R} \times [-\pi, \pi[$. For a fixed (χ, θ), we denote by $\Omega_{\mathcal{R}}(\chi, \theta) \subset \Omega_x$ the domain of definition of $\mathcal{R}(x, \chi, \zeta, \theta)$. The domain of definition $\Omega_{\mathcal{R}}$ actually does not depend on the buoy elevation ζ since it is a vertical shift.

Let us give some examples of the previous mathematical objects in particular cases:

- In the case of a discal solid with radius r, since the geometry is independent of the rotation, it reads

  $$S^{dis}(x, z, \theta) = x^2 + z^2 - r^2 \qquad \text{and} \qquad \underline{\mathcal{S}}^{dis}(x, \theta) = -\sqrt{r^2 - x^2}.$$

  The domain of definition is given by

  $$\Omega_{\mathcal{R}}^{dis}(\chi, \theta) = \{x \in \Omega_x \mid \chi - r < x < \chi + r\}.$$

- In the case of an elliptical solid with semi-minor and semi-major axis respectively equal to a and b, it reads

  $$S^{ell}(x, z, \theta) = \frac{(x\cos\theta + z\sin\theta)^2}{a^2} + \frac{(x\sin\theta - z\cos\theta)^2}{b^2} - 1$$

  and $\underline{\mathcal{S}}^{ell}(x, \theta)$ is the smaller root of the second order polynomial $P_{x,\theta}(z) = S^{ell}(x, z, \theta)$. The domain of definition reads

  $$\Omega_{\mathcal{R}}^{ell}(\chi, \theta) = \left\{x \in \Omega_x \mid \chi + \min_{\vartheta \in [-\pi, \pi[} f_\theta(\vartheta) < x < \chi + \max_{\vartheta \in [-\pi, \pi[} f_\theta(\vartheta)\right\}$$

  with $f_\theta(\vartheta) = a\cos(\theta)\cos(\vartheta) + b\sin(\theta)\sin(\vartheta)$.

Since there is not always an analytical expression for $\mathcal{R}$, we will indicate in Section 3.4 how to handle the problem from a practical point of view.

We are now able to write more precisely the assumption on the surface pressure.

Hypothesis 1. *The pressure varies only on the inferior surface of the solid, i.e. there exists a function $\underline{p}(x, t)$ such that for any $0 \le t \le T$ the surface pressure reads*

$$p(x, z, t) = \begin{cases} \underline{p}(x, t) & \text{if } x \in \mathring{\Omega}_{\mathcal{R}}(\chi(t), \theta(t)) \text{ and } z = \underline{\mathcal{S}}(x, \theta(t)) \\ 0 & \text{else.} \end{cases}$$

In addition, on the inferior surface $\mathring{\Omega}_{\mathcal{R}}(\chi(t), \theta(t))$, the roof $\mathcal{R}$ is regular.

Note that the pressure can still vanish on the inferior surface of the solid when $\underline{p}(x, t) = 0$.

Proposition 1. *Assume that Hypothesis 1 is satisfied.*
Then the movement of the solid body is described by the system

$$C_1 \ddot{\Lambda} = \mathfrak{F}\left(\Lambda, \dot{\Lambda}, t\right) \tag{4}$$

$$\textit{with} \quad \Lambda = \begin{pmatrix} \chi \\ \zeta \\ \theta \end{pmatrix}, \quad C_1 = \begin{pmatrix} M & 0 & 0 \\ 0 & M & 0 \\ 0 & 0 & \mathcal{J} \end{pmatrix} \quad \textit{and} \quad \mathfrak{F} = \mathfrak{F}_E + \mathfrak{F}_P$$

$$\textit{where} \quad \mathfrak{F}_E = \begin{pmatrix} -\displaystyle\int_{\Omega_{\mathcal{R}}} \underline{p}\ \partial_x \mathcal{R}\, \mathrm{d}x + F_\chi \\ \displaystyle\int_{\Omega_{\mathcal{R}}} \underline{p}\ \mathrm{d}x + F_\zeta \\ \displaystyle\int_{\Omega_{\mathcal{R}}} \underline{p}\ \partial_\theta \mathcal{R}\, \mathrm{d}x + T_\theta \end{pmatrix} \quad \textit{and} \quad \mathfrak{F}_P = \begin{pmatrix} 0 \\ -Mg \\ 0 \end{pmatrix}$$

completed with the given initial conditions $\chi(0) = \chi^0$, $\dot{\chi}(0) = \dot{\chi}^0$, $\zeta(0) = \zeta^0$, $\dot{\zeta}(0) = \dot{\zeta}^0$, $\theta(0) = \theta^0$ *and* $\dot{\theta}(0) = \dot{\theta}^0$.

Proof. A general planar motion of a rigid body can be separated into a translational motion of a point in the body and a rotational motion around an axis through that point. It is generally convenient to choose this point as the center of mass G, see [24]. The translational motion can be described by Newton's second law of motion. Taking into account the forces F_χ, F_ζ, the weight together with the pressure applied on the solid from the water gives the following equations

$$\begin{cases} M\ddot{\chi} = \displaystyle\int_{\Omega_{\mathcal{R}}} \underline{p}\ n \cdot e_x \sqrt{1 + (\partial_x \mathcal{R})^2}\, \mathrm{d}x + F_\chi \\ M\ddot{\zeta} = -Mg + \displaystyle\int_{\Omega_{\mathcal{R}}} \underline{p}\ n \cdot e_z \sqrt{1 + (\partial_x \mathcal{R})^2}\, \mathrm{d}x + F_\zeta \end{cases} \tag{5}$$

with n the interior unit normal to the solid surface. The rotational movement is described by the angular momentum theorem, i.e.

$$\partial_t \mathcal{L}_G = \int_{\Omega_{\mathcal{R}}} \underline{p}\, (GX \times n) \sqrt{1 + (\partial_x \mathcal{R})^2}\, \mathrm{d}x + T_\theta \tag{6}$$

where $\mathcal{L}_G$ denotes the angular momentum around G, X a point at the surface with coordinates $(X_x, \mathcal{R}(X_x, \chi, \zeta, \theta))$. By definition of the kinetic momentum in the plane, we have $\partial_t \mathcal{L}_G = \mathcal{J}\ddot{\theta}$. Replacing the inward normal $n = \dfrac{1}{\sqrt{1 + (\partial_x \mathcal{R})^2}} \begin{pmatrix} -\partial_x \mathcal{R} \\ 1 \end{pmatrix}$ in (5) leads to the first two equations of (4) and for (6) it yields

$$\mathcal{J}\ddot{\theta} = -\int_{\Omega_{\mathcal{R}}} \underline{p}\, (GX \cdot e_z \partial_x \mathcal{R} + GX \cdot e_x)\, \mathrm{d}x + T_\theta. \tag{7}$$

Let us denote by $\widetilde{X}_x = X_x - \chi$ the horizontal coordinate in the frame centered on G. In this frame, the movement is a simple rotation of angle θ and as a consequence the coordinates $\left(\widetilde{X}_x, \underline{\mathcal{S}}\left(\widetilde{X}_x, \theta\right)\right)$ of the point X verify

$$\begin{pmatrix} \widetilde{X}_x \\ \underline{\mathcal{S}}\left(\widetilde{X}_x, \theta\right) \end{pmatrix} = M_{\theta - \theta^0} \begin{pmatrix} \widetilde{X}_x^0 \\ \underline{\mathcal{S}}\left(\widetilde{X}_x^0, \theta^0\right) \end{pmatrix}$$

with $\left(\widetilde{X}_x^0, \underline{\mathcal{S}}\left(\widetilde{X}_x^0, \theta^0\right)\right)$ the coordinates of the point X with an angle θ^0 and the matrix of rotation

$$M_\vartheta = \begin{pmatrix} \cos\vartheta & \sin\vartheta \\ -\sin\vartheta & \cos\vartheta \end{pmatrix}. \tag{8}$$

The previous relation implies

$$\underline{\mathcal{S}} = \partial_\theta \widetilde{X}_x. \tag{9}$$

Moreover the trajectory of the points of the solid are concentric circles, i.e. $\partial_\theta \|GX\| = 0$. Thus

$$\partial_\theta \left(\widetilde{X}_x^2 + \left(\underline{\mathcal{S}}\left(\widetilde{X}_x, \theta\right)\right)^2\right) = 0$$

and it follows

$$\widetilde{X}_x \partial_\theta \widetilde{X}_x + \underline{\mathcal{S}} \partial_\theta \widetilde{X}_x \partial_x \underline{\mathcal{S}} + \underline{\mathcal{S}} \partial_\theta \underline{\mathcal{S}} = 0.$$

Using now the relation (9), we get

$$\widetilde{X}_x + \underline{\mathcal{S}} \partial_x \underline{\mathcal{S}} + \partial_\theta \underline{\mathcal{S}} = 0. \tag{10}$$

Finally introducing this relation in (7) and noticing that $GX \cdot e_z = \underline{\mathcal{S}}$ and $GX \cdot e_x = \widetilde{X}_x$ gives the last equation in (4). □

Note that the derivatives of the inferior surface elevation $\partial_x \mathcal{R}$ and $\partial_\theta \mathcal{R}$ are not well-defined at the boundary of its domain of definition $\Omega_{\mathcal{R}}$. However, thanks to Hypothesis 1, the support of the pressure $\underline{p}$ does not reach the boundary of the domain where the inferior surface is defined $\overline{\Omega}_{\mathcal{R}}$. Assuming that the inferior surface elevation $\mathcal{R}$ is regular enough on the support of the pressure $\underline{p}$, we ensure that the integrals in (4) are well-defined.

The solid system admits the following energy balance law.

Lemma 2.2. *The solution of (4) satisfies the following energy law*

$$\partial_t E = \left(\int_{\Omega_{\mathcal{R}}} \underline{p}\, \mathrm{d}x + F_\zeta\right)\dot{\zeta} - \left(\int_{\Omega_{\mathcal{R}}} \underline{p}\partial_x \mathcal{R}\ \mathrm{d}x - F_\chi\right)\dot{\chi} + \left(\int_{\Omega_{\mathcal{R}}} \underline{p}\partial_\theta \mathcal{R}\, \mathrm{d}x + T_\theta\right)\dot{\theta}$$

with the mechanical energy of the buoy $E\left(\dot{\chi}, \dot{\zeta}, \dot{\theta}, \zeta\right) = \dfrac{M}{2}\left(\dot{\zeta}^2 + \dot{\chi}^2\right) + \dfrac{\mathcal{J}}{2}\dot{\theta}^2 + Mg\zeta.$

Proof. Multiplying the first equation of (4) by $\dot{\chi}$, the second equation by $\dot{\zeta}$, the third equation by $\dot{\theta}$ and summing gives the result. □

2.3. **Full system.** Let us now present the coupling of the solid dynamics with the fluid model. According to Newton's third law, i.e. the action-reaction principle, the action of the buoy on the water is opposite to the reaction of the water on the buoy. In the mathematical description introduced previously, it implies that for any $0 \le t \le T$ and $x \in \Omega_{\mathcal{R}}\left(\chi(t), \theta(t)\right)$ we have

$$\underline{p}(x,t) = \overline{p}(x,t). \tag{11}$$

Let us design by $\mathrm{supp}(f)$ the support of the function f. Hypothesis 1 and (11) together leads to the following assumption.

Hypothesis 2. *We assume that the water does not reach the extremities of the buoy, i.e. for any* $0 \le t \le T$

$$\mathrm{supp}\left(\overline{p}(\cdot, t)\right) \subset \mathring{\Omega}_{\mathcal{R}}\left(\chi(t), \theta(t)\right).$$

From now on, we will only use the unknown $\overline{p}$ and we assume that Hypothesis 2 is satisfied.

In the part of the domain where there is no buoy, the roof is defined high enough not to touch the fluid surface and otherwise the roof is given by $\mathcal{R}$. More precisely for $\Pi \in \mathbb{R}$ large enough (in practice we set $\Pi = 10^{40}$) we define

$$R(x,t) = \begin{cases} \mathcal{R}(x, \chi(t), \zeta(t), \theta(t)) & \text{if } x \in \Omega_{\mathcal{R}}(\chi(t), \theta(t)) \\ \Pi & \text{elsewhere.} \end{cases} \tag{12}$$

An energy law for the coupled fluid-solid system (1)-(2)-(4)-(11)-(12) is obtained.

Proposition 2. *Considering a no-flux boundary on Ω_x, any smooth solution of (1)-(2)-(4)-(11)-(12) satisfies the following energy balance law*

$$\partial_t\left(\overline{\mathcal{E}} + E\right) = \int_{\Omega_x} (\rho g h + \overline{p})\, \partial_t B \, \mathrm{d}x + F_\zeta \dot{\zeta} + F_\chi \dot{\chi} + T_\theta \dot{\theta}$$

with $\overline{\mathcal{E}} = \int_{\Omega_x} \mathcal{E} \ \mathrm{d}x$.

Proof. It follows from (3) and (12) that

$$\begin{aligned} \partial_t R(x,t) &= \dot{\chi}\partial_\chi \mathcal{R}(x,\chi,\zeta,\theta) + \dot{\zeta}\partial_\zeta \mathcal{R}(x,\chi,\zeta,\theta) + \dot{\theta}\partial_\theta \mathcal{R}(x,\chi,\zeta,\theta) \\ &= -\dot{\chi}\partial_x \mathcal{R}(x,\chi,\zeta,\theta) + \dot{\zeta} + \dot{\theta}\partial_\theta \mathcal{R}(x,\chi,\zeta,\theta). \end{aligned} \tag{13}$$

Now integrating the energy balance law from Lemma 2.1 over Ω_x and summing with the result from Lemma 2.2 concludes the proof. □

3. Numerical approximation

This section is devoted to the numerical approximation of a solution of (1)-(2)-(4)-(11)-(12). We first describe separately the numerical methods chosen for each model before considering their coupling.

3.1. Discretization for the fluid dynamic.

The 1D mesh is built from the increasing sequence $x_{k+\frac{1}{2}} \in \mathbb{R}$ with $k \in \mathbb{T} \subset \mathbb{N}$. A control volume is an interval $V_k = \left[x_{k-\frac{1}{2}}, x_{k+\frac{1}{2}}\right]$ and we denote by $\ell_k = x_{k+\frac{1}{2}} - x_{k-\frac{1}{2}}$ its length and by $x_k = \frac{x_{k-\frac{1}{2}} + x_{k+\frac{1}{2}}}{2}$ the coordinate of its center. In addition, the time of simulation $[0,T]$ is discretized by $t^{n+1} = t^n + \delta_t^{n+1}$, with $t^0 = 0$, $t^N = T$ and the time step δ_t^{n+1} will be adapted to the flow through a CFL condition see (19) below. The mean value of the bottom level in the control volume V_k, at time t^n, is denoted by B_k^n.

Let us firstly recall the numerical strategy proposed in [18] for the congested shallow water model (1)-(2). A pseudo-compressibility method is used, with λ the relaxation parameter, to take into account the congestion constraint and a low-Froude scheme is used to ensure a good behavior when λ is small enough. Following [18], one particularity of the proposed scheme is that the numerical unknowns are ϕ_k^n and $\overline{u}_k^n$ which are respectively the approximation of the average of the potential defined by

$$\phi = g(h + B) + \frac{\overline{p}}{\rho} \tag{14}$$

and the velocity $\overline{u}$ in the control volume V_k at time t^n. The potential can be used as a parametrization of the water depth and the surface pressure, thus we set

$$\mathcal{H}(\phi, B, R) = \begin{cases} \dfrac{\phi}{g} - B, & \text{if } \phi \leq gR \\ \dfrac{R - B + \lambda^2\left(\frac{\phi}{g} - B\right)}{1+\lambda^2}, & \text{else} \end{cases} \tag{15}$$

$$\text{and} \quad \mathcal{P}(\phi, B, R) = \rho\left(\phi - g\left(\mathcal{H}(\phi, B, R) + B\right)\right).$$

For readability, we set

$$h_k^n = \mathcal{H}(\phi_k^n, B_k^n, R_k^n) \qquad \text{and} \qquad \overline{p}_k^n = \mathcal{P}(\phi_k^n, B_k^n, R_k^n). \tag{16}$$

where R_k^n is an approximation of the mean value of the roof level in the control volume V_k at time t^n. Note that in the present work, R_k^n depends on the discrete values of χ, ζ and θ in a similar way to the continuous case (3), see more detail in Section 3.2. We also introduce the following notation

$$\partial_t^{n+1}\psi = \frac{\psi^{n+1} - \psi^n}{\delta_t^{n+1}} \qquad \text{and} \qquad (\psi)_\pm = \frac{|\psi| \pm \psi}{2}.$$

The scheme finally reads

$$h_k^{n+1} = h_k^n - \frac{\delta_t^{n+1}}{\ell_k}\left(\mathcal{F}_{k+\frac{1}{2}}^{n+1} - \mathcal{F}_{k-\frac{1}{2}}^{n+1}\right) \tag{17}$$

$$\begin{aligned} h_k^{n+1}\overline{u}_k^{n+1} = {} & h_k^n\overline{u}_k^n - \delta_t^{n+1}h_k^{n+1}\frac{\phi_{k+1}^{n+1} - \phi_{k-1}^{n+1}}{2\ell_k} \\ & - \frac{\delta_t^{n+1}}{\ell_k}\left(\overline{u}_k^n\left(\mathcal{F}_{k+\frac{1}{2}}^{n+1}\right)_+ - \overline{u}_{k+1}^n\left(\mathcal{F}_{k+\frac{1}{2}}^{n+1}\right)_-\right) \\ & - \frac{\delta_t^{n+1}}{\ell_k}\left(\overline{u}_k^n\left(\mathcal{F}_{k-\frac{1}{2}}^{n+1}\right)_- - \overline{u}_{k-1}^n\left(\mathcal{F}_{k-\frac{1}{2}}^{n+1}\right)_+\right) \end{aligned} \tag{18}$$

with $\mathcal{F}_{k+\frac{1}{2}}^{n+1}$ an approximation of the mean mass flux $h\overline{u}$ through the interface at $x_{k+\frac{1}{2}}$ between the times t^n and t^{n+1}. More precisely, the numerical flux of the CPR scheme [33] reads

$$\mathcal{F}_{k+\frac{1}{2}}^{n+1} = \frac{h_k^{n+1}\overline{u}_k^n + h_{k+1}^{n+1}\overline{u}_{k+1}^n}{2} - \frac{\gamma\delta_t^{n+1}}{2}\left(\frac{h_k^{n+1}}{\ell_k} + \frac{h_{k+1}^{n+1}}{\ell_{k+1}}\right)\frac{\phi_{k+1}^{n+1} - \phi_k^{n+1}}{2}$$

with a regularization parameter $\gamma \geq 0$ characteristic of the scheme. The numerical scheme requires boundary conditions which depend on the regime of the flow. In the current work, we do not deal with the theoretical issues of the boundary conditions. More precisely, we assume that the flow in not congested at the boundary, i.e. $h_k^n < R_k^n - B_k^n$. It follows that classical boundary conditions of the shallow water model can be used, see [29, Section 21.8].

The following energy dissipation law has been proven in [18, Proposition 2.3].

Lemma 3.1. *Let $\gamma \geq 1$ and assume that for any $k \in \mathbb{T}$ and any $0 \leq n < N$ the following CFL condition is satisfied*

$$\left(\left| \frac{\overline{u}_k^n + \overline{u}_{k+1}^n}{2} \right| + \sqrt{\frac{\gamma}{2}} \sqrt{\left| \frac{\phi_{k+1}^{n+1} - \phi_k^{n+1}}{2} \right|} \right) \delta_t^{n+1} \leq \frac{\min\left(h_k^{n+1}, h_{k+1}^{n+1}\right)}{2\left(h_k^{n+1} + h_{k+1}^{n+1}\right)} \min\left(\ell_k, \ell_{k+1}\right). \tag{19}$$

Then the scheme (17) admits the following energy dissipation law

$$\partial_t^{n+1} \mathcal{E}_k + \frac{1}{\ell_k}\left(\mathcal{G}_{k+\frac{1}{2}}^{n+1} - \mathcal{G}_{k-\frac{1}{2}}^{n+1}\right) \leq -\overline{p}_k^{n+1} \partial_t^{n+1} R_k + \left(\rho g h_k^n + \overline{p}_k^{n+1}\right) \partial_t^{n+1} B_k \tag{20}$$

with the discrete mechanical energy

$$\mathcal{E}_k^n = \rho\left(\frac{1}{2} h_k^n \left(\overline{u}_k^n\right)^2 + g h_k^n \left(B_k^n + \frac{h_k^n}{2}\right) + \frac{g}{2\lambda^2}\left(h_k^n - R_k^n + B_k^n\right)_+^2\right)$$

and the numerical energy flux

$$\begin{aligned} \mathcal{G}_{k+\frac{1}{2}}^n = \rho & \left(\frac{\left|\overline{u}_k^n\right|^2}{2} \left(\mathcal{F}_{k+\frac{1}{2}}^{n+1}\right)_+ - \frac{\left|\overline{u}_{k+1}^n\right|^2}{2} \left(\mathcal{F}_{k+\frac{1}{2}}^{n+1}\right)_- \right) + \frac{\phi_k^{n+1} + \phi_{k+1}^{n+1}}{2} \mathcal{F}_{k+\frac{1}{2}}^{n+1} \\ & - \frac{h_{k+1}^{n+1} \overline{u}_{k+1}^n - h_k^{n+1} \overline{u}_k^n}{2} \frac{\phi_{k+1}^{n+1} - \phi_k^{n+1}}{2} \\ & + \delta_t^{n+1} \left(\frac{h_{k+1}^{n+1}}{\ell_{k+1}} - \frac{h_k^{n+1}}{\ell_k} \right) \left| \frac{\phi_{k+1}^{n+1} - \phi_k^{n+1}}{2} \right|^2. \end{aligned}$$

3.2. **Discretization for the solid dynamic.** The current section is devoted to the numerical approximation of a solution of the solid dynamics (4). The approximation of the three degrees of freedom χ, ζ and θ of the solid at time t^n are respectively denoted by χ^n, ζ^n and θ^n. Due to its simple implementation, a Newmark scheme is chosen. For $(\alpha, \beta) \in [0,1]^2$, the Newmark scheme for an ODE of the form $C_1 \ddot{\Lambda} = \mathfrak{F}\left(\Lambda, \dot{\Lambda}, t\right)$ writes

$$\begin{cases} \Lambda^{n+1} = \Lambda^n + \delta_t^{n+1} \dot{\Lambda}^n + \dfrac{\left(\delta_t^{n+1}\right)^2}{2}\left(\beta \ddot{\Lambda}^{n+1} + (1-\beta)\,\ddot{\Lambda}^n\right) \\ \dot{\Lambda}^{n+1} = \dot{\Lambda}^n + \delta_t^{n+1}\left(\alpha \ddot{\Lambda}^{n+1} + (1-\alpha)\,\ddot{\Lambda}^n\right). \end{cases} \tag{21}$$

In our case, we have $\Lambda = (\chi, \zeta, \theta)^T$ while C_1 and $\mathfrak{F}$ are given in (4). The scheme reads $C_1 \ddot{\Lambda}^n = \mathfrak{F}_P + \mathfrak{F}_E^n$ with

$$\mathfrak{F}_E^n = \begin{pmatrix} -\displaystyle\sum_{k \in \mathbb{T}} \ell_k \overline{p}_k^n \partial_x^k R^{n-1} + F_\chi^n \\ \displaystyle\sum_{k \in \mathbb{T}} \ell_k \overline{p}_k^n + F_\zeta^n \\ \displaystyle\sum_{k \in \mathbb{T}} \ell_k \overline{p}_k^n \partial_\theta^k R^{n-1} + T_\theta^n \end{pmatrix} \tag{22}$$

where $\partial_x^k R^n$ (resp. $\partial_\theta^k R^n$) are discretizations of the derivative of the roof with respect to x (resp. θ) at time t^n in the control volume V_k. These terms will be discussed below in order to obtain the energy stability for the coupled fluid-solid

model. In the following, we take $\alpha = \beta = 1$. This choice is motivated by the fact that the surface pressure source term in (20) is implicit and it is required to get the discrete energy stability, see Proposition 4 below. With this choice, the Newmark scheme is completely implicit and expected to be first order accurate.

At the discrete level, the Hypothesis 1 and Hypothesis 2 are not required for the stability of the scheme but must be considered for the relevance of the simulation result. It is actually similar to the case of discontinuous bottom in a classical shallow water model.

Let us first state the energy stability for the Newmark scheme.

Lemma 3.2. *For any $0 \leq n < N$ the scheme (21)-(22) satisfies the following energy law*

$$\partial_t^{n+1} E \quad = \quad \mathfrak{F}_E^{n+1} \cdot \partial_t^{n+1} \Lambda \tag{23}$$

with $E^n = E\left(\dot{\chi}^n, \dot{\zeta}^n, \dot{\theta}^n, \zeta^n\right)$ defined in Lemma 2.2.

Proof. The proof for the general ODE case is detailed in [25, Section 3]. Using a Newmark scheme for the linear equation of motion on a vector of unknowns Λ

$$C_1 \ddot{\Lambda}^n + C_2 \dot{\Lambda}^n + C_3 \Lambda^n = \mathfrak{F}^n$$

where C_1, C_2 and C_3 are matrices and $\mathfrak{F}^n$ a given vector, the following energy equation is proven

$$\begin{aligned}\partial_t^{n+1}\left(\frac{1}{2}\dot{\Lambda}\cdot\left(C_1 + \frac{\delta_t^{n+1}}{2}C_2\right)\dot{\Lambda} + \frac{1}{2}\Lambda\cdot C_3\Lambda\right) &= \partial_t^{n+1}\Lambda\cdot\mathfrak{F}^{n+1} \\ -\frac{1}{2}\partial_t^{n+1}\Lambda\cdot\left(C_2 + \delta_t^{n+1}C_3\right)\partial_t^{n+1}\Lambda &- \frac{1}{2}\left(\frac{\dot{\Lambda}^{n+1}+\dot{\Lambda}^n}{2}\cdot C_2\frac{\dot{\Lambda}^{n+1}+\dot{\Lambda}^n}{2}\right).\end{aligned}$$

With the definition given in Proposition 1, the following estimate holds

$$\partial_t^{n+1}\left(\frac{1}{2}\dot{\Lambda}\cdot C_1\dot{\Lambda}\right) = \partial_t^{n+1}\Lambda\cdot\left(\mathfrak{F}_P + \mathfrak{F}_E^{n+1}\right) = -\partial_t^{n+1}\left(Mg\zeta\right) + \partial_t^{n+1}\Lambda\cdot\mathfrak{F}_E^{n+1}.$$

The time evolution of the mechanical energy reads

$$\partial_t^{n+1}E = \partial_t^{n+1}\left(\frac{M}{2}\left(\dot{\zeta}^2 + \dot{\chi}^2\right) + \frac{\mathcal{J}}{2}\dot{\theta}^2 + Mg\zeta\right) = \partial_t^{n+1}\left(\frac{1}{2}\dot{\Lambda}\cdot C_1\dot{\Lambda}\right) + \partial_t^{n+1}\left(Mg\zeta\right).$$

Summing the two previous equalities leads to (23). □

3.3. **Coupling strategy between the fluid and the solid.** Let us now concentrate on the discrete coupling. We will discuss the form of $\partial_x^k R^n$ and $\partial_\theta^k R^n$ in (22) and analyze the energy of the coupled system. First an estimate of the discrete entropy law for a general discretization of the operators $\partial_x R^n$ and $\partial_\theta R^n$ is given. In a second paragraph an adapted choice for $\partial_x^k R^n$ and $\partial_\theta^k R^n$ is proposed to ensure the entropy stability of the numerical scheme.

3.3.1. *A first entropy estimate.* In this section, we consider the following straightforward discretization of $\partial_x R^n$ and $\partial_\theta R^n$

$$\begin{aligned}&\partial_{xC}^k R^n = \frac{R_{k+1}^n - R_{k-1}^n}{2\ell_k} \\ \text{and}\quad &\partial_{\theta C}^k R^n = -\left(x_k - \chi^n\right) - \left(R_k^n - \zeta^n\right)\partial_{xC}^k R^n.\end{aligned} \tag{24}$$

The discrete operator $\partial^k_{xC} R^n$ is the centered discretization of $\partial_x \mathcal{R}$ and the discretization of $\partial^k_{\theta C} R^n$ comes from (10). More precisely $\partial^k_{\theta C} R^n$ is a discretization of $-(X_x - \chi) - (\mathcal{R} - \zeta)\,\partial_x \mathcal{R}$.

A discrete energy inequality for the coupled fluid-solid system can be written.

Proposition 3. *Consider a no-flux boundary on Ω_x. Under the CFL condition (19) the scheme (17)-(21)-(22) with any discretized operators $\partial^k_x R^n$ and $\partial^k_\theta R^n$, admits for any $0 \leq n < N$ the following energy inequality*

$$\begin{aligned}\partial_t^{n+1}\left(\overline{\mathcal{E}} + E\right) \leq \sum_{k\in\mathbb{T}} \left(\ell_k \left(\rho g h_k^n + \overline{p}_k^{n+1}\right) \partial_t^{n+1} B_k\right) \\ + F_\zeta^{n+1} \partial_t^{n+1}\zeta - F_\chi^{n+1}\partial_t^{n+1}\chi + T_\theta^{n+1}\partial_t^{n+1}\theta \\ + \sum_{k\in\mathbb{T}} \ell_k \overline{p}_k^{n+1}\left(-\partial_t^{n+1} R_k - \partial_t^{n+1}\chi \partial_x^k R^n + \partial_t^{n+1}\zeta + \partial_t^{n+1}\theta \partial_\theta^k R^n\right)\end{aligned}$$

with $\overline{\mathcal{E}}^n = \sum_{k\in\mathbb{T}} \ell_k \mathcal{E}_k^n$.

Proof. Summing (20) over the computational domain and adding (23) gives the result. □

The estimate of Proposition 3 is general in the sense that it holds for any discrete operators $\partial^k_x R^n$ and $\partial^k_\theta R^n$. In addition, it is consistent with the continuous energy estimate given in Proposition 2 since using classical arguments and thanks to (13) the last term vanishes when the space step and the time step goes to zero. However the last term does not vanish and its sign cannot be determined in general and in particular for the discrete operators (24).

3.3.2. *Numerical discretization ensuring entropy stability.* Let us now discuss a discretization for $\partial_x R^n$ and $\partial_\theta R^n$ such that the energy stability is ensured. We set

$$\begin{aligned}\partial^k_{xE} R^n &= \begin{cases} -\dfrac{R_k^{n+1} - \mathcal{R}\left(x_k, \chi^n, \zeta^{n+1}, \theta^{n+1}\right)}{\chi^{n+1} - \chi^n}, & \text{if } \chi^{n+1} \neq \chi^n \\ \partial^k_{xC} R^n, & \text{else} \end{cases} \\ \text{and} \quad \partial^k_{\theta E} R^n &= \begin{cases} \dfrac{\mathcal{R}\left(x_k, \chi^n, \zeta^n, \theta^{n+1}\right) - R_k^n}{\theta^{n+1} - \theta^n}, & \text{if } \theta^{n+1} \neq \theta^n \\ \partial^k_{\theta C} R^n, & \text{else.} \end{cases}\end{aligned} \tag{25}$$

With the discrete operator (25), the discrete counterpart of the energy dissipation law Proposition 2 can be proven.

Proposition 4. *Consider a no-flux boundary on Ω_x. Under the CFL condition (19) the scheme (17)-(21)-(22) with $\partial^k_x R^n = \partial^k_{xE} R^n$ and $\partial^k_\theta R^n = \partial^k_{\theta E} R^n$ given by (25) admits for any $0 \leq n < N$ the following dissipation law*

$$\begin{aligned}\partial_t^{n+1}\left(\overline{\mathcal{E}} + E\right) \leq \sum_{k\in\mathbb{T}} \left(\ell_k \left(\rho g h_k^n + \overline{p}_k^{n+1}\right) \partial_t^{n+1} B_k\right) \\ + F_\zeta^{n+1} \partial_t^{n+1}\zeta - F_\chi^{n+1}\partial_t^{n+1}\chi + T_\theta^{n+1}\partial_t^{n+1}\theta.\end{aligned}$$

Proof. Assume first the unknowns χ and θ at two successive time steps are not the same, i.e. $\chi^{n+1} \neq \chi^n$ and $\theta^{n+1} \neq \theta^n$. With the discrete operators (25) the last term of the estimate of Proposition 3 reads

$$\begin{aligned}&\delta_t^{n+1}\left(\partial_t^{n+1} R_k + \partial_t^{n+1}\chi \partial^k_{xE} R^n - \partial_t^{n+1}\zeta - \partial_t^{n+1}\theta \partial^k_{\theta E} R^n\right) \\ &\quad = \left(R_k^{n+1} - R_k^n\right) - \left(R_k^{n+1} - \mathcal{R}\left(x_k, \chi^n, \zeta^{n+1}, \theta^{n+1}\right)\right) \\ &\qquad - \left(\zeta^{n+1} - \zeta^n\right) - \left(\mathcal{R}\left(x_k, \chi^n, \zeta^n, \theta^{n+1}\right) - R_k^n\right) \\ &\quad = \left(\mathcal{R}\left(x_k, \chi^n, \zeta^{n+1}, \theta^{n+1}\right) - \mathcal{R}\left(x_k, \chi^n, \zeta^n, \theta^{n+1}\right)\right) - \left(\zeta^{n+1} - \zeta^n\right).\end{aligned}$$

Using (3) we conclude that this term vanishes. Otherwise, if $\chi^{n+1} = \chi^n$ (resp. if $\theta^{n+1} \neq \theta^n$) the evolution of the mechanical energy does not depend on $\partial_x^k R^n$ (resp. $\partial_\theta^k R^n$). So any well defined and consistent discretization can be used in this case without affecting the mechanical energy estimate. We conclude that the using the discretization (25), the reminder of Proposition 3 and the discrete energy dissipation is ensured. □

3.4. **Practical details.** Some details about the practical implementation are given below.

3.4.1. *Buoy implementation.* The discretization of the roof $\mathcal{R}(x, \chi, \zeta, \theta)$ is defined from the buoy surface written under the form $\mathcal{S}(x, z, \theta) = 0$, see (3). However in practice, the geometry of a realistic buoy is not in general parametrized in this form. Let us explain in the following the numerical implementation of the discrete roof $\mathcal{R}^\delta(x, \chi, \zeta, \theta)$ the geometry of a buoy with a general shape in a one-dimensional framework.

In practice the buoy is represented thanks to a finite sequence $\mathcal{S}_0^\delta$ of N_P points $(X_i, Z_i)_{0\leq i\leq N_P-1}^t$. The points describe the vertices of a polygon approaching the geometry of the buoy in the frame centered on the center of mass. For a set of variables $\Lambda = (\chi, \zeta, \theta)$, the buoy is described by the sequence of points

$$\mathcal{S}^\delta(\chi, \zeta, \theta) = \left\{ M_\theta \begin{pmatrix} X \\ Z \end{pmatrix} + \begin{pmatrix} \chi \\ \zeta \end{pmatrix} \mid \begin{pmatrix} X \\ Z \end{pmatrix} \in \mathcal{S}_0^\delta \right\}$$

where the rotation matrix M_θ is defined in (8).

Let $\underline{i}$ (resp. $\overline{i}$) be the index of the point of the buoy at the left (resp. at the right) extremity, i.e.

$$\underline{i}(\chi, \zeta, \theta) = \max_{0\leq i\leq N_P-1} \{\forall j, 0 \leq j \leq N_P - 1,\ X_i \leq X_j\}$$

$$\text{and} \quad \overline{i}(\chi, \zeta, \theta) = \min_{0\leq i\leq N_P-1} \{\forall j, 0 \leq j \leq N_P - 1,\ X_i \geq X_j\}.$$

The inferior surface elevation in the frame of the buoy is defined by the subsequence

$$\begin{aligned} &\underline{\mathcal{S}}^\delta(\chi, \zeta, \theta) = \left\{ \left(X_{I_i(\chi,\zeta,\theta)}, Z_{I_i(\chi,\zeta,\theta)}\right)^t \in \mathcal{S}^\delta(\chi, \zeta, \theta) \ \mid 0 \leq i \leq J(\chi, \zeta, \theta) \right\} \\ \text{with} \quad &I_i(\chi, \zeta, \theta) = i + \underline{i}(\chi, \zeta, \theta) \mod N_P \\ \text{and} \quad &J(\chi, \zeta, \theta) = \overline{i}(\chi, \zeta, \theta) - \underline{i}(\chi, \zeta, \theta) \mod N_P. \end{aligned}$$

For any position x not under the buoy, i.e. $x < X_{\underline{i}(\chi,\zeta,\theta)}$ or $x > X_{\overline{i}(\chi,\zeta,\theta)}$, we set $\mathcal{R}^\delta(x, \chi, \zeta, \theta) = \Pi$, see (12). In the part of the domain where the buoy is, i.e. $X_{\underline{i}(\chi,\zeta,\theta)} \leq x \leq X_{\overline{i}(\chi,\zeta,\theta)}$, the roof is deduced by linear interpolation from the points in $\underline{\mathcal{S}}^\delta(\chi, \zeta, \theta)$. More precisely, let

$$\begin{aligned} \underline{i}_x(\chi, \zeta, \theta) &= \max_{i\in\mathbb{I}(\chi,\zeta,\theta)} \left\{X_{I_i(\chi,\zeta,\theta)} \leq x\right\} \\ \text{and} \quad \overline{i}_x(\chi, \zeta, \theta) &= \min_{i\in\mathbb{I}(\chi,\zeta,\theta)} \left\{X_{I_i(\chi,\zeta,\theta)} \geq x_k\right\}. \end{aligned}$$

In other words, $\left(X_{I_{\underline{i}_x(\chi,\zeta,\theta)}}, Z_{I_{\underline{i}_x(\chi,\zeta,\theta)}}\right)^t$ (resp. $\left(X_{I_{\overline{i}_x(\chi,\zeta,\theta)}}, Z_{I_{\overline{i}_x(\chi,\zeta,\theta)}}\right)^t$) is among the sequence of points $\underline{\mathcal{S}}^\delta(\chi, \zeta, \theta)$ the nearest vertex from the left (respectively from

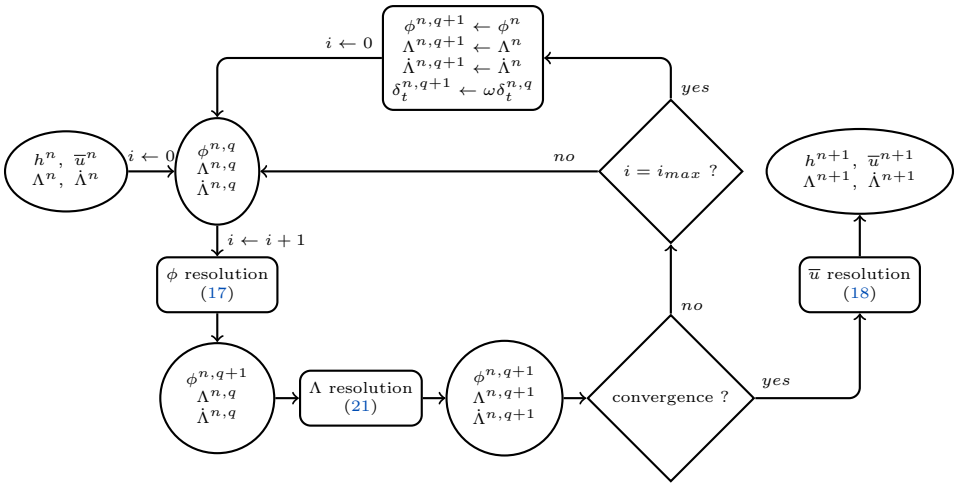

FIGURE 2. Scheme of the weak coupling iterative process.

the right) to x. To get an approximation of the roof a linear interpolation is done, i.e.

$$\mathcal{R}^\delta(x,\chi,\zeta,\theta) = \frac{\left(x - X_{I_x(\chi,\zeta,\theta)}\right) Z_{I_{\bar{i}_x(\chi,\zeta,\theta)}} + \left(X_{I_{\bar{i}_x(\chi,\zeta,\theta)}} - x\right) Z_{I_{i_x(\chi,\zeta,\theta)}}}{X_{I_{\bar{i}_x(\chi,\zeta,\theta)}} - X_{I_{i_x(\chi,\zeta,\theta)}}}.$$

In the following test cases, the discrete roof is estimated using this strategy, i.e. $R_k^n = \mathcal{R}^\delta(x_k, \chi^n, \zeta^n, \theta^n)$, and in the discrete operators (25), we use $\mathcal{R}^\delta(x,\chi,\zeta,\theta)$ instead of $\mathcal{R}(x,\chi,\zeta,\theta)$.

3.4.2. *Fixed point approach.* The scheme (17) is implicit and non-linear, see [33]. Because of the derivative of the roof in the dynamic equation of the buoy, the computation of the Jacobian required to apply a Newton method is not trivial. In order to easily introduce new forces on the buoy, we propose a weak coupling iterative process where the buoy and the water dynamics are solved successively until convergence. In addition, the CFL condition (19) does not take into account the buoy dynamics. A time step adaptation is added to reduce the time step when the convergence of the iterative process is too slow. The reader can find more details on time step adaptation in [13] for example. The iterative process is precisely described in the following. In practice the fixed point algorithm converges in a few iterations (less than 20) with reasonable time steps, but this observation depends on the test case. The rigorous proof of convergence for the fixed point is out of the scope of this work.

Let us describe more precisely the iterative process, illustrated in Figure 2. We consider the state $\left((h_k^n, \overline{u}_k^n)_{k\in\mathbb{T}}, \Lambda^n, \dot{\Lambda}^n\right)$ given with $\Lambda = (\chi,\zeta,\theta)$. Let the exponent q relating to the iteration number of the iterative process. The iterative process is initialized by $\phi_k^{n,0}$ computed from h_k^n using (14), $\Lambda^{n,0} = \Lambda^n$ and $\dot{\Lambda}^{n,0} = \dot{\Lambda}^n$. To obtain the next approximation $q+1$ from the approximation q, first we compute the potential $\phi_k^{n,q+1}$ considering the roof $R_k^{n,q}$ obtained from the buoy position $\Lambda^{n,q}$, see Section 3.4.1. From the new potential, we compute the surface pressure $\overline{p}_k^{n,q+1}$

using (15) and (16). This pressure is then used to compute the external force for the computation of the buoy dynamics (21). At this step, we get an approximation of the state variable $\left(h_k^n, \Lambda^n, \dot{\Lambda}^n\right)$ at time t^{n+1}, that does not necessarily satisfy the constraint (2). To impose the constraint on each time step, the previous operations are repeated until numerical convergence. Two stopping criteria are used to increase the reliability of the result, based on the L^∞-norm of the residual of the non-linear system (17) (already used in the case without structure see [33]) and the L^∞-norm of the difference between two iterations of the buoy variable Λ. When the two errors estimate are inferior to a tolerance ε_{New}, we consider the fixed point as converged. Finally, the velocity $\overline{u}_k^{n+1}$ is estimated using (18).

Except when the vertical velocity of the buoy is large, the convergence of the iterative process is acceptable (less than 20 iterations). However, when the vertical velocity of the buoy is large and especially when it reaches the water surface, convergence can be hard. To avoid two-way wiring in the fixed point, the time step is limited if too many iterations are required. More precisely, we set a maximum acceptable number of iterations i_{max} in the fixed point. If the Newton iterative process reaches the number of iterations i_{max}, the time step is reduced and the time iteration is recomputed, i.e. $W^{n,q+1} = W^n$ and $\delta_t^{n,q+1} = \omega \delta_t^{n,q}$ with a reduction factor $\omega < 1$. The implicit CFL condition (19) is verified for every time iteration at convergence to ensure the scheme to be entropy satisfying, see Lemma 3.1. If the CFL condition is not verified, the time iteration is recomputed using the time step given by (19).

4. Simulations

We illustrate the validity of our coupled numerical model by some one dimensional computations. In the following we take $g = 9.81$ and $\rho = 1$. The mesh is a regular grid with the space step $\ell_k = \delta_x$. The relaxation parameter is chosen as $\lambda = \sqrt{\delta_x}$, see [18] for more details about this choice. The regularization parameter γ is set to 2. It is slightly increased compared to the optimal value necessary to get the entropy estimate see Lemma 3.1. This has a regularizing effect (see [33]) and prevents oscillations which can be observed with the CPR scheme in the vicinity of a shock.

All the test cases are computed with the different strategies presented above, i.e. (24) and (25). When the difference between the results of the two strategies are not significative, only the result with the entropy-satisfying scheme (25) is illustrated. The numerical parameters (see Section 3.4) are set to $\varepsilon_{New} = 10^{-10}$, $i_{max} = 20$ and $\omega = 0.5$.

Let us give a brief motivation of the following test cases. In Section 4.1 we compare the solution computed with the numerical strategy presented above to an analytical solution established in [26]. This test case emphasizes the convergence of the proposed numerical strategy. However, the two different discretizations (24) and (25) cannot be compared in this context since the horizontal displacement and the rotation of the buoy are frozen, and the two schemes are equivalent in this context. We compare the two different discretizations (24) and (25) in Section 4.2, by performing a test case where all the degrees of freedom of the buoy are free. In addition, this test case emphasizes the robustness of the scheme to detect the regions where the buoy reaches the water. Eventually, in Section 4.3, we propose a

simple but realistic configuration of a wave energy converter to illustrate possible applications of this work.

4.1. **Return to equilibrium.** To illustrate the consistency of the scheme, we compare the computed solution to an analytical solution. In [26, Corollary 1], the analytical solution of a return to equilibrium is established. It corresponds to the vertical movement of a rectangular buoy, of horizontal length L, freely floating above a water initially at rest and with a flat bottom $B = 0$. A similar analytical solution in axisymmetric framework is established in [8]. Note this configuration satisfies neither Hypothesis 1, Hypothesis 2 nor the assumption of the derivation of the fluid equations (1)-(2), see [18, 26]. However, for what concerns the numerical scheme, it can be written without difficulty and this test case validates the accuracy of the method in a dynamic context.

The equilibrium of the system is defined by $\overline{u} = 0$, a fixed $h_{eq} \in \mathbb{R}_+$ and $\zeta = \zeta_{eq}$ such that

$$Mg = \int_{\Omega_x} \overline{p}\,\mathrm{d}x = \rho \int_{\Omega_x} \left(h_{eq} - \left(\underline{\mathcal{S}}\left(x - \chi_{eq}, \theta_{eq}\right) + \zeta_{eq}\right)\right)_+ \mathrm{d}x \tag{26}$$

where $\chi_{eq} \in \mathbb{R}$ and $\theta_{eq} \in [-\pi, \pi]$ are fixed. For simplicity we set $\chi_{eq} = \theta_{eq} = 0$. In other words the equilibrium is the situation where the surface pressure balances out the weight of the buoy. Only a vertical movement is considered for this test case. More precisely we suppose that

$$F_\chi = \int_{\Omega_x} \overline{p}\partial_x \mathcal{R}\,\mathrm{d}x, \qquad T_\theta = -\int_{\Omega_x} \overline{p}\partial_\theta \mathcal{R}\,\mathrm{d}x \qquad \text{and} \qquad F_\zeta = 0 \tag{27}$$

which expresses the fact that the horizontal and angular degrees of freedom are fixed.

Initially the water is at rest so that $h^0 = \min\left(h_{eq}, \underline{\mathcal{S}}\left(x, 0\right) + \zeta^0\right)$ and $\overline{u}^0 = 0$. The length of the roof is $L = 0.8$ and the roof is defined so that it is symmetric with respect to its center of mass. For the above defined configuration, the position of the center of mass is determined by

$$\left(\frac{M}{\rho} + \frac{2}{3\zeta}\left(\frac{L}{2}\right)^3\right)\ddot{\zeta} = -gL\left(\zeta - \zeta_{eq}\right) - \nu\left(\dot{\zeta}\right) + \mu\left(\zeta\right)\dot{\zeta}^2 \tag{28}$$

with the coefficients

$$\nu\left(\dot{\zeta}\right) = gL\left(h_{eq} - \left(\tau\left(\frac{L}{4\sqrt{g}}\dot{\zeta}\right)\right)^2\right) \quad \text{and} \quad \mu\left(\zeta\right) = \frac{4}{3\zeta^2}\left(\frac{L}{2}\right)^3.$$

The coefficient τ is given by $\tau\left(r\right) = \frac{1}{3}\left(\sqrt{h_{eq}} + C\left(r\right) + \frac{h_{eq}}{C(r)}\right)$ with

$$C\left(r\right) = \frac{3}{2}\left(-4r + \frac{8}{27}h_{eq}^{\frac{3}{2}} + 4\sqrt{r\left(r - \frac{4}{27}h_{eq}^{\frac{3}{2}}\right)}\right)^{\frac{1}{3}}.$$

In this test case, we consider a buoy of mass $M = 0.5$ with the equilibrium elevation $\zeta_{eq} = 1$ and the water depth h_{eq} computed to satisfy (26). Initially the state of the buoy is $\zeta^0 = 1.2$ and $\dot{\zeta}^0 = 0$. For the computation, we set $\Omega_x = [-20, 20]$ with wall condition at boundaries.

The simulation is compared to the solution of (28) in Figure 3, where $\delta_G = \zeta - \zeta_{eq}$. The agreement between the two solutions is good and the solution tends to the

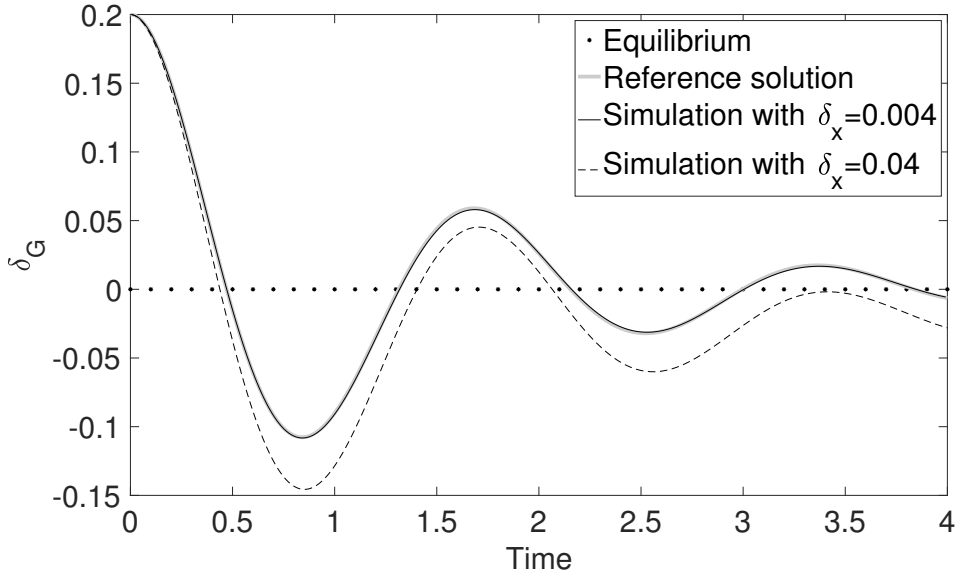

FIGURE 3. Return to equilibrium: time evolution of the distance to the equilibrium position $\delta_G = \zeta - \zeta_{eq}$

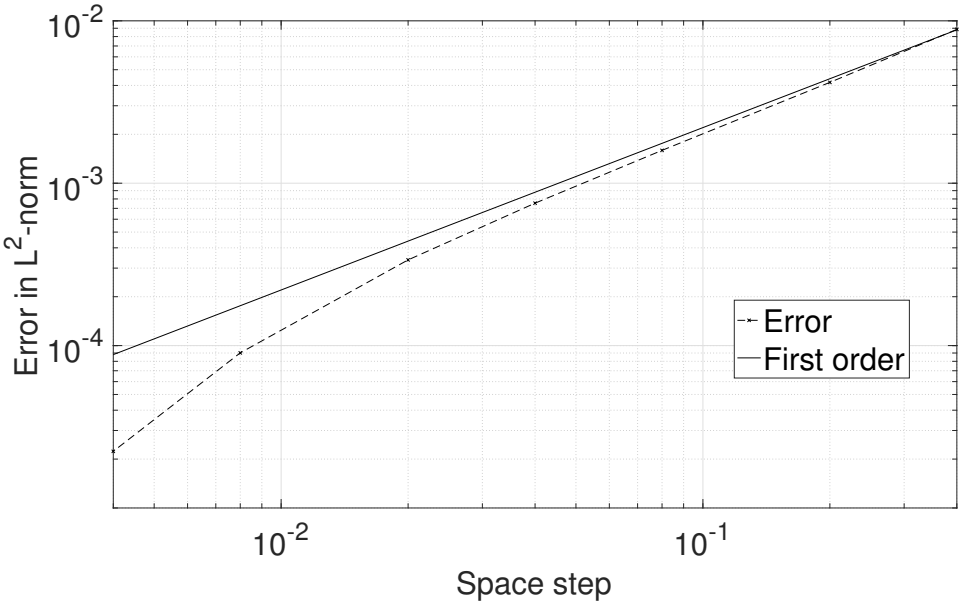

FIGURE 4. Return to equilibrium: Convergence rate in L^2-norm for δ_G.

equilibrium position as expected. The convergence rate in norm L^2 in time until the end of the simulation (here fixed to 4) of δ_G is shown in Figure 4. A convergence rate slightly better than one is observed. We recall that a first order scheme is expected since the full implicit Newmark scheme and the fluid scheme are first order.

Remark 1. *Because of the symmetry of the test case, the external forces actually read* $F_\chi = T_\theta = 0$. *However, this equilibrium is unstable since small perturbations, such as those introduce by the machine errors, break the symmetry. For this reason, even with an axisymmetric buoy, the external forces* (27) *are imposed.*

4.2. **Throwing.** To illustrate the robustness of the scheme, we propose the simulation of a buoy thrown into the water. This simulation can be compared to a block of ice falling in water from an iceberg, except that the parameters such as the mass and the angular moment are not physically relevant.

We consider a closed domain $\Omega_x = [0, 2]$ with wall boundary conditions and a flat bottom $B = 0$. The water is initially at rest, i.e. $h^0 = 1$ and $\overline{u}^0 = 0$. The buoy is defined following the strategy explained in Section 3.4.1 with

$$\mathcal{S}_0^\delta = \left\{ \begin{pmatrix} X \\ Z \end{pmatrix} \left(\frac{i}{N_P} 2\pi \right) \ , \quad 0 \leq i \leq N_P - 1 \right\} \ ,$$
$$\begin{pmatrix} X \\ Z \end{pmatrix} = \begin{pmatrix} 0.3\cos(\vartheta) + 0.03\cos(4\vartheta) \\ 0.2\sin(\vartheta) - 0.03\cos(4\vartheta) - 0.06 \end{pmatrix} \ ,$$

its mass is $M = 10^{-2}$ and its angular moment is $\mathcal{J} = 10^{-2}$. We do not consider any additional force, i.e. $F_\chi = F_\zeta = T_\theta = 0$. The initial state of the buoy is $\chi^0 = 0$, $\zeta^0 = 1.5$, $\theta^0 = \frac{\pi}{2}$ $\dot{\chi}^0 = 1$, $\dot{\zeta}^0 = 1$ and $\dot{\theta}^0 = 0$.

In Figure 5, the buoy position, the water height and the surface pressure at different times are shown with the numerical parameters $\delta_x = 10^{-3}$ and $N_P = 360$. At the beginning the fluid is at rest and the buoy is not in contact with the fluid. At the impact an energy transfer from the buoy to the water is observed and waves are created. It is easy to verify that the non-penetration constraint (2) is qualitatively met, more precisely at the order λ, see [18]. Let us consider the mechanical energy $\overline{\mathcal{E}}^n + E^n$ without the potential energy of the water at rest $\overline{\mathcal{E}}^0$ and normalized by the energy of the buoy at the initial state E^0, i.e.

$$e^n = \frac{\overline{\mathcal{E}}^n + E^n - \overline{\mathcal{E}}^0}{E^0}.$$

At the initial state, the main part of the energy of the system is the potential energy of the water. By removing the potential energy of the water at rest, the direction of energy variation is unchanged but the amplitude of the variation is significantly increased.

The evolution of the energy ratio e^n is shown in Figure 6 (first line) for both discretizations (24) and (25) and for two different space steps. Accordingly to the theoretical result Proposition 4, the mechanical energy is decreasing for the discretization (25). In practice the centered discretization (24) leads to satisfactory results except for coarse resolution. With $\delta_x = 10^{-2}$, the mechanical energy is increasing at time $t = 1.5$ and the results is significantly affected, in particular for the horizontal position, see Figure 6 (second line).

4.3. **Wave energy converter.** To illustrate the ability of the strategy to optimize a wave energy converter, a restoring and a damping force are introduced, see Figure 7. The structure is allowed to move vertically and to rotate around its center of mass and it is fixed in the horizontal direction, i.e. $F_\zeta = -c\dot{\zeta} - \kappa\left(\zeta - \overline{\zeta}\right)$, $T_\theta = 0$ and $F_\chi = \int_{\Omega_x} \overline{p}\partial_x \mathcal{R}\, \mathrm{d}x$. The damping (resp. stiffness) coefficients are denoted by $c \in \mathbb{R}_+$ (resp. $\kappa \in \mathbb{R}_+$). The equilibrium length of the spring is denoted by $\overline{\zeta}$. Let us rewrite

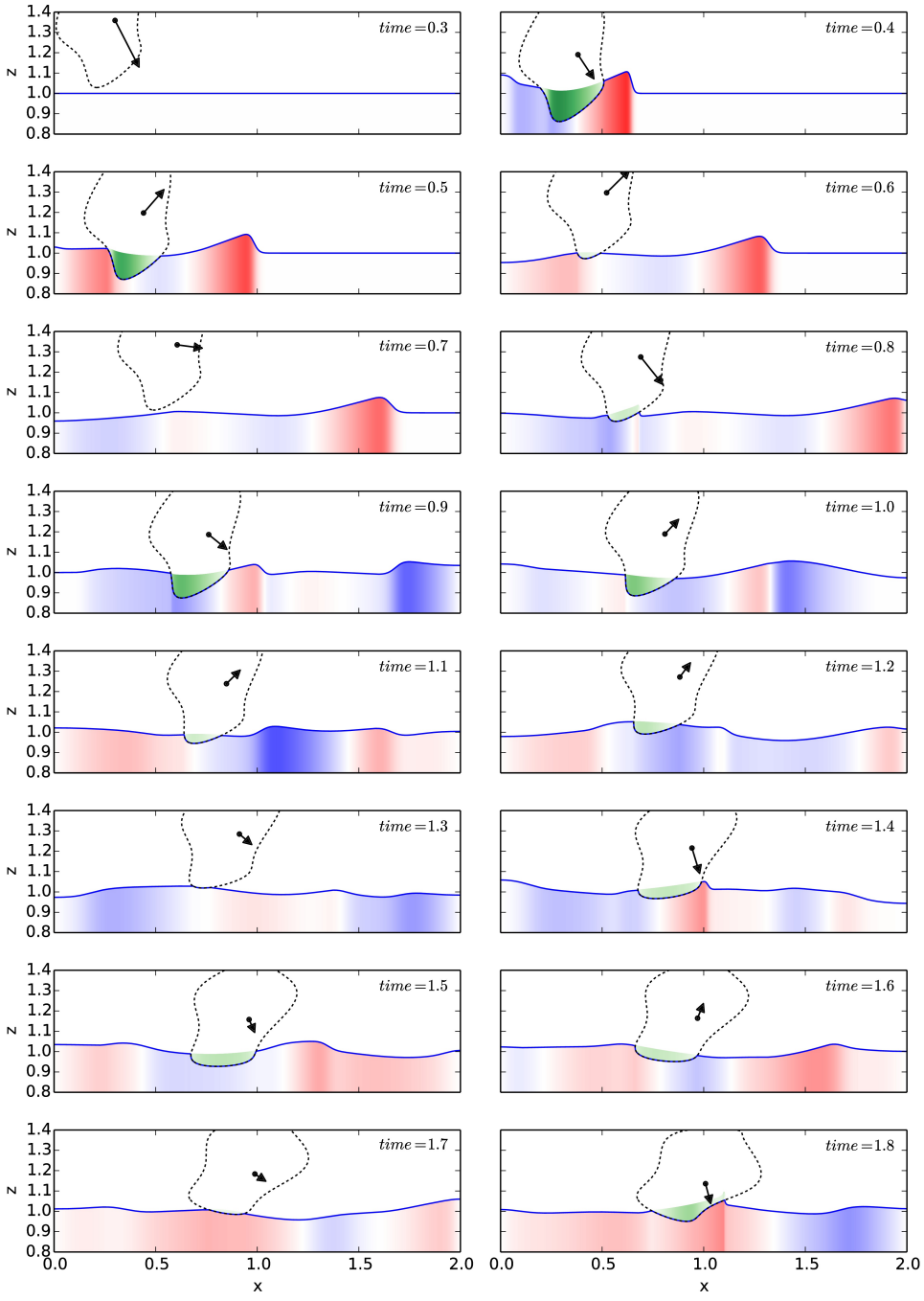

FIGURE 5. Throwing: Buoy (black dotted line), water height (blue solid line), velocity (filled surface in the water – blue$<0<$red) and surface pressure (green filled surface in the buoy) at several times.

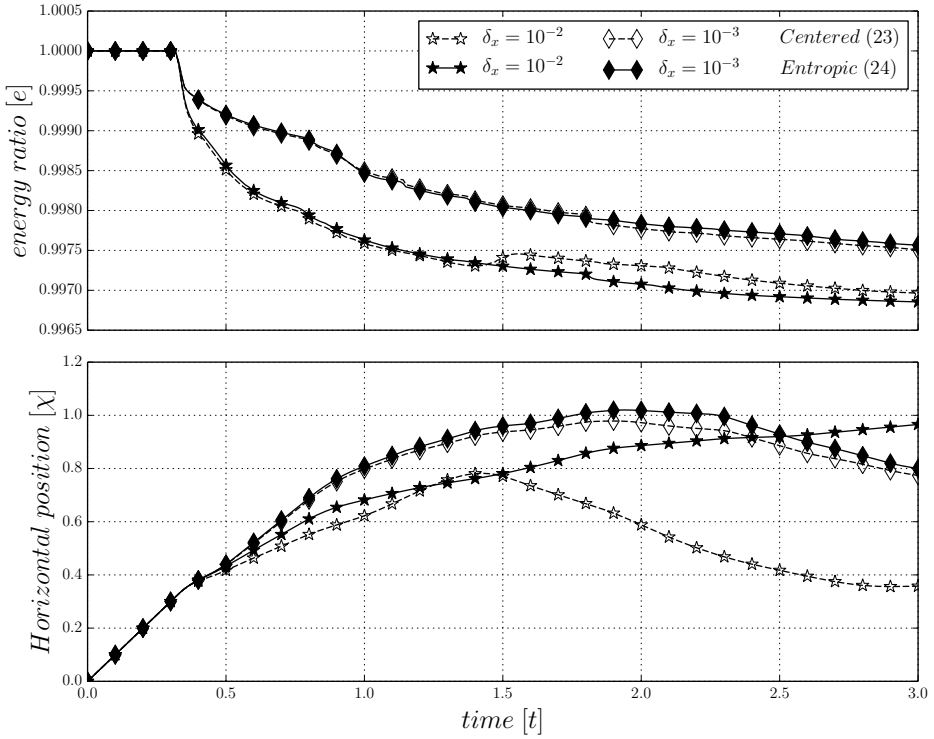

FIGURE 6. Throwing: Mechanical energy (first line) and buoy horizontal position (second line) evolutions.

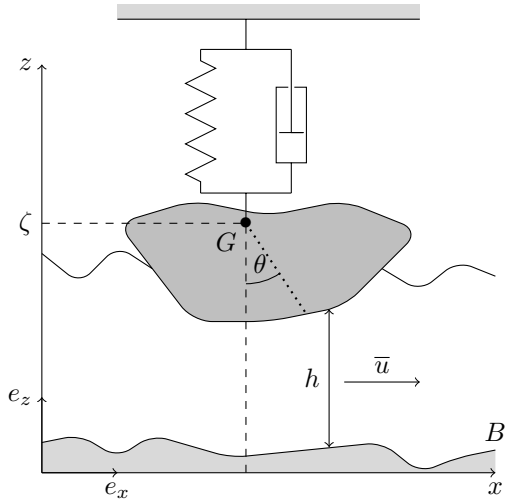

FIGURE 7. Wave energy converter with a spring

the equations from Section 2.2 in the case where we add a spring. The proofs of the following results are not detailed since they are simple adaptations of Lemma 3.2 and Proposition 4.

The planar movement of the energy wave converter is described by the system

$$\left\{\begin{array}{l} M\ddot{\zeta} = -Mg + \displaystyle\int_{\Omega_x} \underline{p}\,\mathrm{d}x - c\dot{\zeta} - \kappa\left(\zeta - \overline{\zeta}\right) \\ \mathcal{J}\ddot{\theta} = \displaystyle\int_{\Omega_x} \underline{p}\partial_\theta \mathcal{R}\,\mathrm{d}x. \end{array}\right. \tag{29}$$

The following energy estimates can be obtained

Lemma 4.1. *The solution of (29) satisfies the following energy law*

$$\partial_t \widetilde{E} = \int_{\Omega_x} \underline{p}\partial_\theta \mathcal{R}\,\mathrm{d}x\dot{\theta} + \int_{\Omega_x} \underline{p}\,\mathrm{d}x\dot{\zeta} - c\dot{\zeta}^2$$

with $\widetilde{E}(\zeta,\theta) = \dfrac{\mathcal{J}}{2}\dot{\theta}^2 + \dfrac{M}{2}\dot{\zeta}^2 + Mg\zeta + \dfrac{\kappa}{2}\left(\zeta - \overline{\zeta}\right)^2$.

Proposition 5. *Considering a no-flux boundary on Ω_x, any smooth solution of (1)-(2)-(11)-(12)-(29) satisfies the following energy balance law*

$$\partial_t\left(\overline{\mathcal{E}} + \widetilde{E}\right) = \int_{\Omega_x} \left(\overline{p} + \rho g h\right)\partial_t B\,\mathrm{d}x - P_c \qquad \text{with} \qquad P_c = c\dot{\zeta}^2.$$

The term P_c is a dissipation term due to the damping of the spring. A part of this energy could be recovered for energy production.

Using again the Newmark scheme (21) with $\widetilde{\Lambda} = \begin{pmatrix}\zeta\\ \theta\end{pmatrix}$, (29) is discretized in the following way

$$\left\{\begin{array}{l} M\ddot{\zeta}^n = -Mg + \displaystyle\sum_{k\in\mathbb{T}} \ell_k \overline{p}_k^n - c\dot{\zeta}^n - \kappa\left(\zeta^n - \overline{\zeta}\right) \\ \mathcal{J}\ddot{\theta}^n = \displaystyle\sum_{k\in\mathbb{T}} \ell_k \overline{p}_k^n \partial_\theta^k R^{n-1}. \end{array}\right. \tag{30}$$

The following discrete estimates can be obtained

Lemma 4.2. *The scheme (21)-(30) satisfies for any $0 \le n < N$ the following energy law*

$$\begin{array}{rcl} \partial_t^{n+1}\left(\widetilde{E} + \dfrac{\delta_t^{n+1}}{4}\left(\dot{\zeta}\right)^2\right) & = & \displaystyle\sum_{k\in\mathbb{T}} \left(\ell_k \overline{p}_k^{n+1}\partial_\theta^k R^n\right)\partial_t^{n+1}\theta + \sum_{k\in\mathbb{T}} \ell_k \overline{p}_k^n \partial_t^{n+1}\zeta \\ & & -P_c^{n+1} - \kappa\dfrac{\delta_t^{n+1}}{2}\left(\partial_t^{n+1}\zeta\right)^2 \end{array}$$

with $\widetilde{E}^n = \widetilde{E}\left(\zeta^n,\theta^n\right)$ *and* $P_c^{n+1} = \dfrac{c}{2}\left(\left(\partial_t^{n+1}\zeta\right)^2 + \left(\dfrac{\dot{\zeta}^{n+1} + \dot{\zeta}^n}{2}\right)^2\right)$.

Proof. The proof is similar to the proof of Lemma 3.2. The coefficients are (with obvious notations)

$$\widetilde{f}^n = \begin{pmatrix} -Mg + \kappa\overline{\zeta} + \displaystyle\sum_{k\in\mathbb{T}} \ell_k \overline{p}_k^n \\ \displaystyle\sum_{k\in\mathbb{T}} \ell_k \overline{p}_k^n \partial_\theta^k R^{n-1} \end{pmatrix}, \qquad \widetilde{C}_1 = \begin{pmatrix} M & 0 \\ 0 & \mathcal{J} \end{pmatrix}, \quad \widetilde{C}_2 = \begin{pmatrix} c & 0 \\ 0 & 0 \end{pmatrix}$$
$$\text{and} \quad \widetilde{C}_3 = \begin{pmatrix} \kappa & 0 \\ 0 & 0 \end{pmatrix}.$$

□

Proposition 6. *Consider a no-flux boundary on Ω_x. Under the CFL condition (19) the scheme (17)-(18)-(21)-(30) with $\partial_\theta^k R^n = \partial_{\theta E}^k R^n$ given by (25) admits for any $0 \leq n < N$ the following dissipation law*

$$\partial_t^{n+1}\left(\overline{\mathcal{E}} + \widetilde{E} + \frac{\delta_t^{n+1}}{4}\left(\dot{\zeta}\right)^2\right) \leq \sum_{k\in\mathbb{T}}\left(\ell_k\left(\rho g h_k^n + \overline{p}_k^{n+1}\right)\partial_t^{n+1} B_k\right) - P_c^{n+1} - \kappa\frac{\delta_t^{n+1}}{2}\left(\partial_t^{n+1}\zeta\right)^2.$$

The optimization of wave energy converters is a key point in the development of such devices. To show the feasibility of an optimization procedure, a naive estimate of the recoverable energy is done. The recovered energy, depending on the technology used to convert wave energy, is a part of the recoverable energy defined by

$$E_c = \sum_{n=1}^{N} \delta_t^n P_c^n$$

where N is the number of time iterations and P_c^n is defined in Lemma 4.2.

In the following a simple case of a wave energy converter attached to a spring over a flat bottom $B = 0$ is simulated. An elliptical shaped buoy with semi-minor and semi-major axis respectively equal to 0.2 and 0.4 is considered, see Section 2.2 for the description of the buoy geometry. The mass is $M = 10^{-2}$ and the moment of inertia $\mathcal{J} = 5 \cdot 10^{-3}$. The stiffness coefficient is $\kappa = 10^{-2}$ and the characteristic elevation is $\overline{\zeta} = 1.4$. Initially, the water and the buoy are at equilibrium. More precisely, the initial state of the buoy reads $\chi = 1.5$, $\zeta = 1.4$, $\theta^0 = \frac{\pi}{2}$, $\dot{\zeta} = 0$ and $\dot{\theta}^0 = 0$, and the water state reads $\overline{u}^0 = 0$ and $h^0 = \min\left(h_{eq}, \underline{\mathcal{S}}\left(x - \chi, \theta^0\right) + \zeta^0\right)$ with h_{eq} so that the buoy is at equilibrium, see (26). The computational domain is $\Omega_x = [0, 3]$. At the left, a fixed water depth boundary condition is considered, see [29, Section 21.8], with $h\left(0, t\right) = h_{eq} + 0.05\sin\left(4\pi t\right)$. At the right boundary a wall boundary condition is considered.

In Figure 8 the ratio between the recoverable energy E_c and the total energy introduced $\mathcal{E}_{tot}$ is shown at time $t = 1$ with the space step $\delta_x = 3 \cdot 10^{-3}$ and for several values of c. The total energy introduced is computed by considering a similar simulation without the buoy. More precisely it is defined by $\mathcal{E}_{tot} = \overline{\mathcal{E}}^N - \overline{\mathcal{E}}^0$.

The recoverable energy E_c is about 10% of the total energy $\mathcal{E}_{tot}$ that is not negligible considering that many parameters can also be optimized (shape, mass and moment of inertia of the buoy). In this case, the best choice seems to be obtained around $c = 0.3$. Physically a small stiffness allows the spring to move as much as possible. Furthermore a small damping coefficient would not be able to absorb any energy. In contrary if the damping coefficient is too high, the buoy will be slowed down due to the damping and the recoverable energy would not be optimal.

5. Conclusion

A strong coupling between a congested shallow water type model and Newton's second law of motion is presented for the modeling of floating structures. We have taken a particular care to the energy transfer between the solid and the

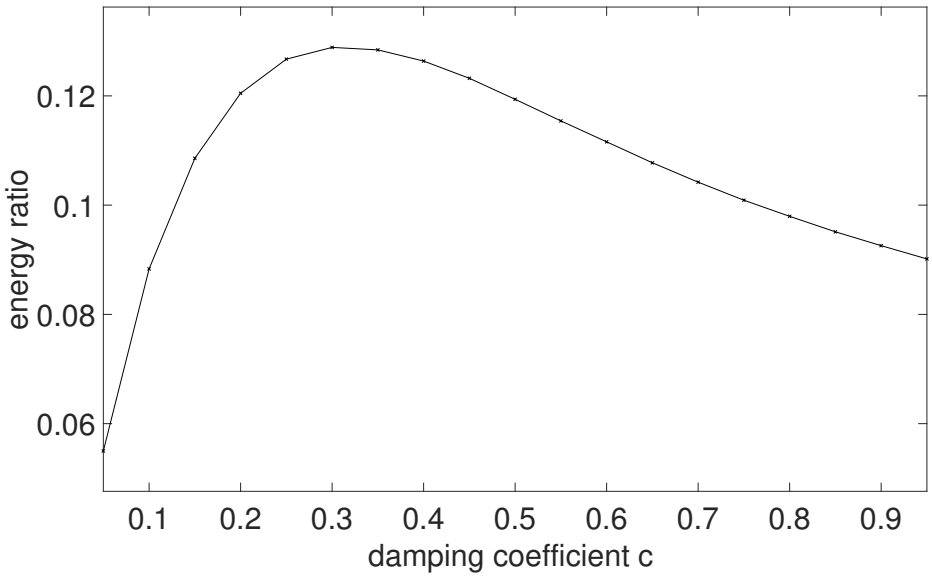

FIGURE 8. Spring: energy ratio for different values of the damping coefficient

water. An entropy correction is made at the discrete level in order to ensure an entropy dissipation law and the numerical scheme proposed in [18] is adapted to take into account a freely floating body. Finally numerical simulations are proposed to validate the approach and to show the feasibility of physically relevant cases.

Now real life applications need an extension to the two dimensional case. Since the computations become CPU costly in higher dimensions, some scientific computing issues should be resolved beforehand. One can think of linking our method with a less CPU consuming scheme for free surface flow far from the congested area.

The physical description of water waves is important when considering wave energy converters. More complex models such as dispersive models [12, 27], layerwise vertical discretization [3] or the combination of both [17] could be used to represent the flow. Dispersive models do not neglect the vertical acceleration and are therefore more adapted to characterize heave effets. In any numerical strategies where the dispersive terms are introduce as a correction of a shallow water scheme [2, 9, 16, 28, 32], the strategy presented in the current work can be use instead of the classical shallow water scheme to obtain floating body modeling with a dispersive model. In addition, a layerwise discretization can better reproduce wind effects and friction on the body by considering a vertical profile of the velocity. We expect that the improvement of our results with a layerwise discretization not raise particular difficulties since the velocity is computed separately to the constraint in the current numerical strategy. Last but not least, our method is directly adaptable to take into account several bodies, as long as no collision between them appear. It is in particular interesting for the simulation and optimization of farms of wave energy converters [35]. A logical follow-up in another direction is to consider the collisions between floating bodies. It should be essential to study the drift of floating fragments during flooding.

Since these phenomena take place on a large space scale, the proposed model seems well adapted. Eventually, a challenging objective is the handling of submerged body [15, 19]. This issue seems not at hand at the moment since a more complex description of the flow is required.

Acknowledgments

The authors wish to express their warm thanks to Cindy Guichard for many fruitful discussions and kind advices. This research is part of a collaborative program with the Anr-Fem (France Energies Marines) project Hyflo-Eflu through the project call ite emr 2015.

References

[1] Agamloh, E., Wallace, A., and von Jouanne, A. Application of fluid-structure interaction simulation of an ocean wave energy extraction device. *Renewable Energy 33*, 4 (2008), 748–757.

[2] Aissiouene, N., Bristeau, M.-O., Godlewski, E., and Sainte-Marie, J. A combined finite volume - finite element scheme for a dispersive shallow water system. *Networks and Heterogeneous Media (NHM)* (Jan. 2016).

[3] Audusse, E., Bristeau, M.-O., Perthame, B., and Sainte-Marie, J. A multilayer Saint-Venant system with mass exchanges for shallow water flows. Derivation and numerical validation. *ESAIM: Mathematical Modelling and Numerical Analysis 45*, 1 (2011), 169–200.

[4] Benyo, K. Wave-structure interaction for long wave models with a freely moving bottom. working paper or preprint <hal-01665775>, 2017.

[5] Benyo, K. Numerical analysis of the weakly nonlinear Boussinesq system with a freely moving body on the bottom. working paper or preprint <arXiv-1805.07216>, 2018.

[6] Bergmann, M., and Iollo, A. Bioinspired swimming simulations. *Journal of Computational Physics 323* (2016), 310 – 321.

[7] Bocchi, E. Floating structures in shallow water: local well-posedness in the axisymmetric case. working paper or preprint <arXiv-1802.07643>, 2018.

[8] Bocchi, E. On the return to equilibrium problem for axisymmetric floating structures in shallow water, 2019.

[9] Bonneton, P., Chazel, F., Lannes, D., Marche, F., and Tissier, M. A splitting approach for the fully nonlinear and weakly dispersive Green–Naghdi model. *Journal of Computational Physics 230*, 4 (2011), 1479–1498.

[10] Bosi, U., Engsig-Karup, A. P., Eskilsson, C., and Ricchiuto, M. A spectral/hp element depth-integrated model for nonlinear wave–body interaction. *Computer Methods in Applied Mechanics and Engineering 348* (2019), 222–249.

[11] Bresch, D., Lannes, D., and Metivier, G. Waves interacting with a partially immersed obstacle in the Boussinesq regime. working paper or preprint <arXiv-1902.04837>, 2019.

[12] Bristeau, M.-O., Mangeney, A., Sainte-Marie, J., and Seguin, N. An energy-consistent depth-averaged Euler system: derivation and properties. *Discrete and Continuous Dynamical Systems - Series B 20*, 4 (2015), 961–988.

[13] Cancès, C., and Guichard, C. Numerical analysis of a robust free energy diminishing finite volume scheme for parabolic equations with gradient structure. *Foundations of Computational Mathematics 17*, 6 (2017), 1525–1584.

[14] Chabannes, V., Pena, G., and Prud'homme, C. High-order fluid–structure interaction in 2d and 3d application to blood flow in arteries. *Journal of Computational and Applied Mathematics 246* (2013), 1 – 9. Fifth International Conference on Advanced COmputational Methods in ENgineering (ACOMEN 2011).

[15] Ducassou, B., Nuñez, J., Cruchaga, M., and Abadie, S. A fictitious domain approach based on a viscosity penalty method to simulate wave/structure interaction. *Journal of Hydraulic Research 55*, 6 (2017), 847–862.

[16] Favrie, N., and Gavrilyuk, S. A rapid numerical method for solving serre–green–naghdi equations describing long free surface gravity waves. *Nonlinearity 30*, 7 (2017), 2718.

[17] Fernández-Nieto, E. D., Parisot, M., Penel, Y., and Sainte-Marie, J. A hierarchy of dispersive layer-averaged approximations of Euler equations for free surface flows. *Communications in Mathematical Sciences 16*, 5 (2018), 1169–1202.

[18] Godlewski, E., Parisot, M., Sainte-Marie, J., and Wahl, F. Congested shallow water model: roof modeling in free surface flow. *ESAIM: Mathematical Modelling and Numerical Analysis 52*, 5 (Sep 2018), 1679–1707.

[19] Guerber, E., Benoit, M., Grilli, S. T., and Buvat, C. A fully nonlinear implicit model for wave interactions with submerged structures in forced or free motion. *Engineering Analysis with Boundary Elements 36*, 7 (2012), 1151 – 1163.

[20] Harris, J., Kuznetsov, K., Peyrard, C., Saviot, S., Mivehchi, A., T. Grilli, S., and Benoit, M. Simulation of wave forces on a gravity based foundation by a BEM based on fully nonlinear potential flow. In *27th Offshore and Polar Engineering Conference* (San Francisco, USA, 2017).

[21] Iguchi, T., and Lannes, D. Hyperbolic free boundary problems and applications to wave-structure interactions. working paper or preprint <arXiv-1806.07704>, 2018.

[22] John, F. On the motion of floating bodies. I. *Communications on Pure and Applied Mathematics 2*, 1 (1949), 13–57.

[23] Kashiwagi, M. Non-linear simulations of wave-induced motions of a floating body by means of the mixed Eulerian-Lagrangian method. *Proceedings of the Institution of Mechanical Engineers, Part C: Journal of Mechanical Engineering Science 214*, 6 (2000), 841–855.

[24] Knudsen, J., and Hjorth, P. *Elements of Newtonian Mechanics*. Springer Berlin Heidelberg, 2012.

[25] Krenk, S. Energy conservation in Newmark based time integration algorithms. *Computer methods in applied mechanics and engineering 195*, 44 (2006), 6110–6124.

[26] Lannes, D. On the dynamics of floating structures. *Annals of PDE 3*, 1 (2017), 11.

[27] Lannes, D., and Bonneton, P. Derivation of asymptotic two-dimensional time-dependent equations for surface water wave propagation. *Physics of Fluids 21*, 1 (2009), 016601.

[28] Lannes, D., and Marche, F. A new class of fully nonlinear and weakly dispersive Green–Naghdi models for efficient 2D simulations. *Journal of Computational Physics 282* (2 2015), 238–268.

[29] LeVeque, R. J. *Finite volume methods for hyperbolic problems*. Cambridge University Press, 2002.

[30] Matt, F., Babarit, A., Ben, C., David, F., Louise, O., Katie, S., Johannes, S., and Troch, P. A review of numerical modelling of wave energy converter arrays. In *ASME 2012 International Conference on Ocean, Offshore and Artic Engineering* (Rio de Janeiro, Brazil, 2012).

[31] Palm, J., Eskilsson, C., Moura Paredes, G., and Bergdahl, L. CFD simulation of a moored floating wave energy converter. In *Proceedings of the 10th European Wave and Tidal Energy Conference* (Aalborg, Denmark, 2013).

[32] Parisot, M. Entropy-satisfying scheme for a hierarchy of dispersive reduced models of free surface flow. *International Journal for Numerical Methods in Fluids 0*, ja.

[33] Parisot, M., and Vila, J.-P. Centered-Potential Regularization for the advection upstream splitting method. *SIAM Journal on Numerical Analysis 54*, 5 (2016), 3083–3104.

[34] Parolini, N., and Quarteroni, A. Mathematical models and numerical simulations for the America's cup. *Computer Methods in Applied Mechanics and Engineering 194*, 9 (2005), 1001–1026.

[35] Penalba, M., Touzón, I., Lopez-Mendia, J., and Nava, V. A numerical study on the hydrodynamic impact of device slenderness and array size in wave energy farms in realistic wave climates. *Ocean Engineering 142* (2017), 224–232.

[36] Quarteroni, A., Tuveri, M., and Veneziani, A. Computational vascular fluid dynamics: problems, models and methods. *Computing and Visualization in Science 2*, 4 (2000), 163–197.

[37] Wu, G., and Taylor, R. The coupled finite element and boundary element analysis of nonlinear interactions between waves and bodies. *Ocean Engineering 30*, 3 (2003), 387–400.

[38] Yu, Y.-H., and Li, Y. Reynolds-averaged Navier–Stokes simulation of the heave performance of a two-body floating-point absorber wave energy system. *Computers & Fluids 73* (2013), 104–114.

E-mail address: edwige.godlewski@sorbonne-universite.fr
E-mail address: martin.parisot@inria.fr
E-mail address: jacques.sainte-marie@inria.fr
E-mail address: fabien.wahl@inria.fr

Sorbonne Université, université Paris-Diderot SPC, CNRS, Inria, laboratoire Jacques-Louis Lions, LJLL, ANGE team, F-75005 Paris, France